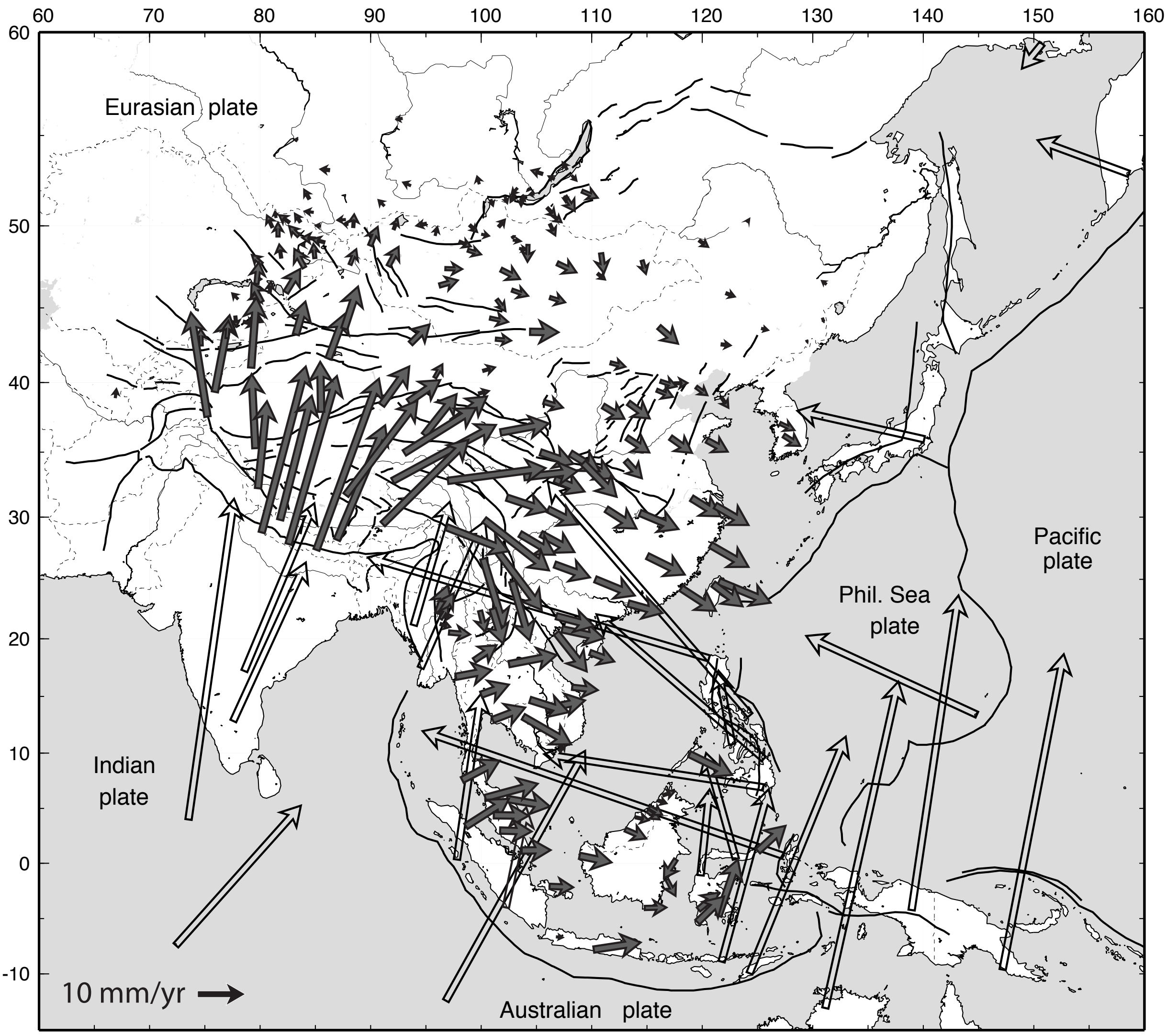

Figure 2. GPS velocities with respect to Eurasia. Only sites with velocity uncertainty less than 1.5 mm/yr (95% confidence) are used and shown here. Solid arrows show GPS site velocities withing Asia, open arrows show velocity of neighboring plates.

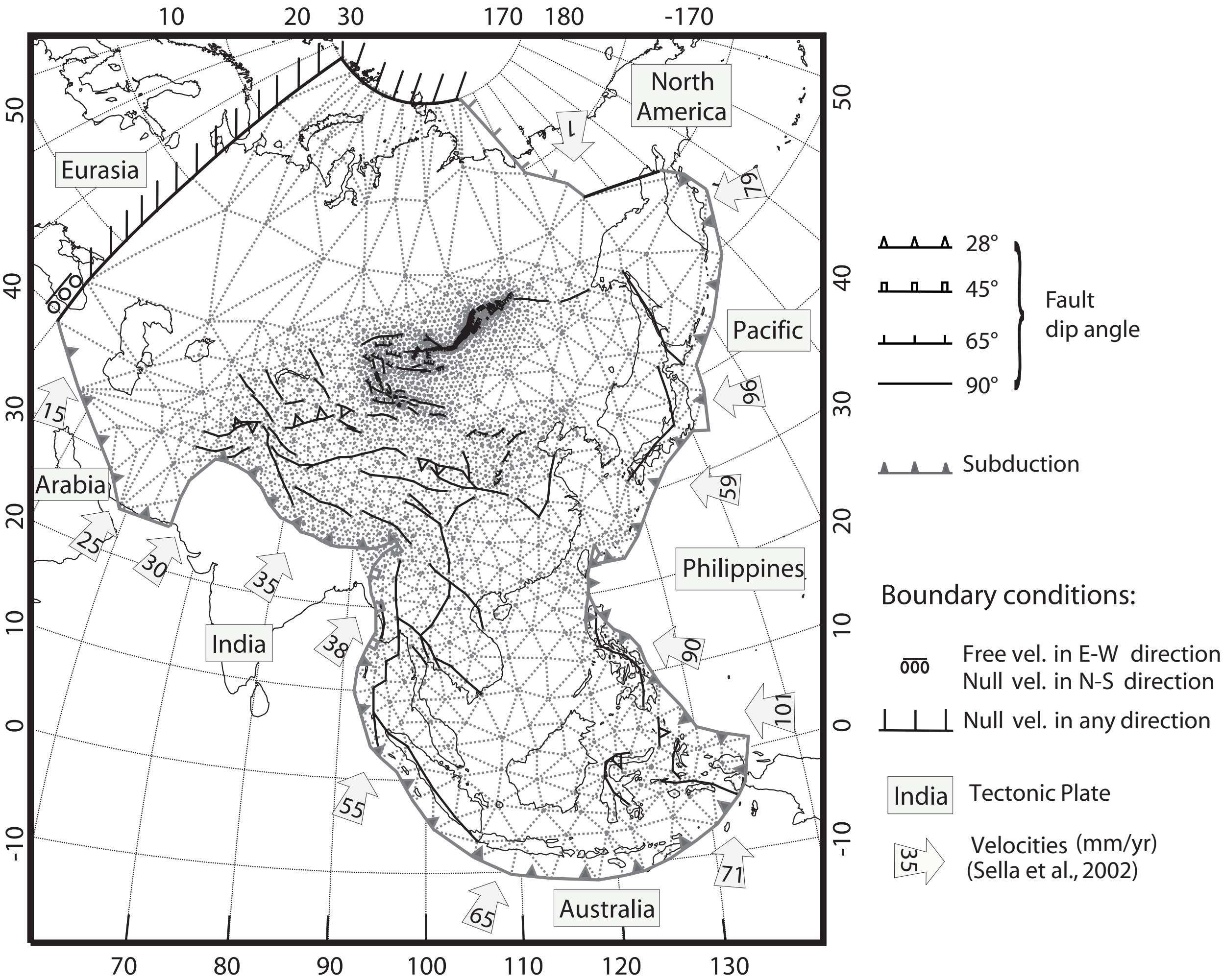

Figure 3. Finite element grid, boundary conditions, and faults used in the models.

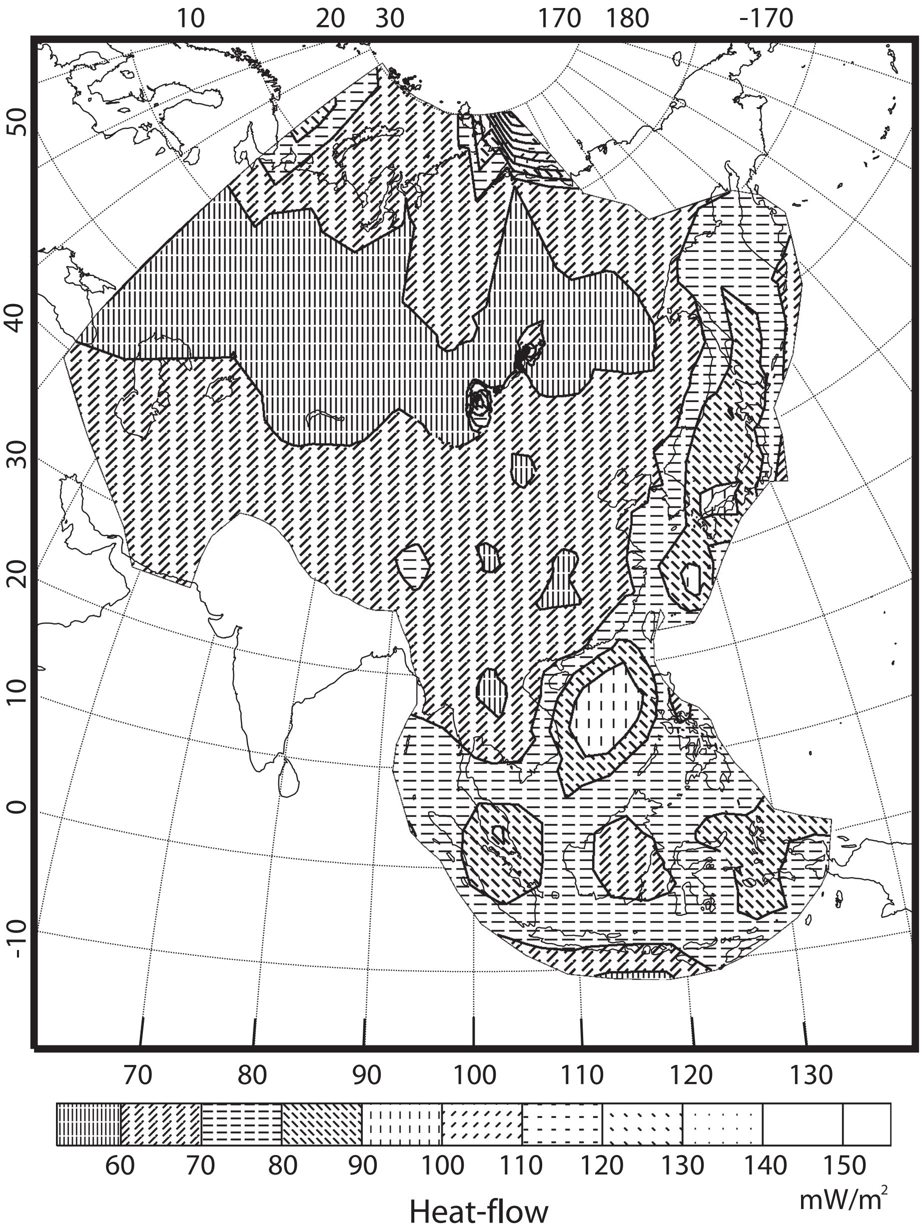

Figure 4. Map of surface heat flow used in the models. Heat flow data comes from the worldwide database compiled by *Pollack et al.* [1993] and from *Lysak* [1992] for the Mongolia-Baikal area, resampled and interpolated on a 5°x5°grid for most of the study area, except in the Mongolia-Baikal area, where we used a 12'x12' grid.

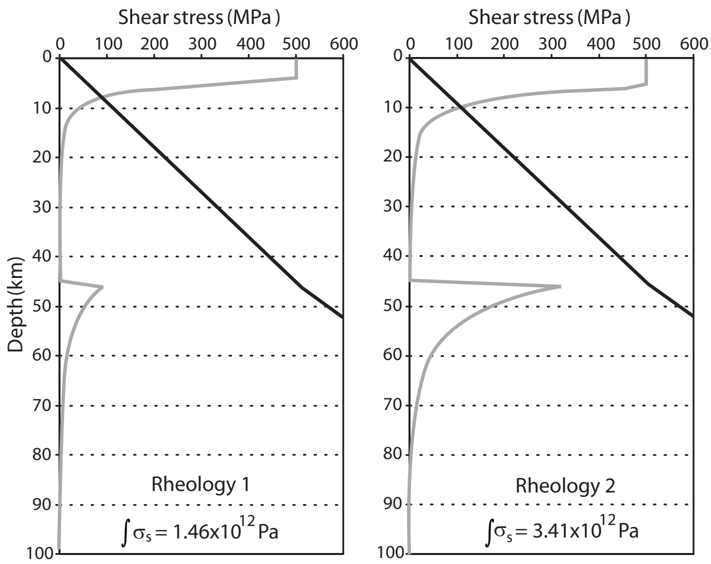

Figure 5. Examples of rheological profiles for a 45 km thick crust and a 0.059 W m^2 surface heat flow obtained using the thermal thermal parameters listed in Table 1, with $\mu = 0.85$, and $\dot{\varepsilon} = 3 \times 10^{-16}/s$. Black lines shows frictional sliding, grey line is for non-Newtonian thermally activated dislocation creep.

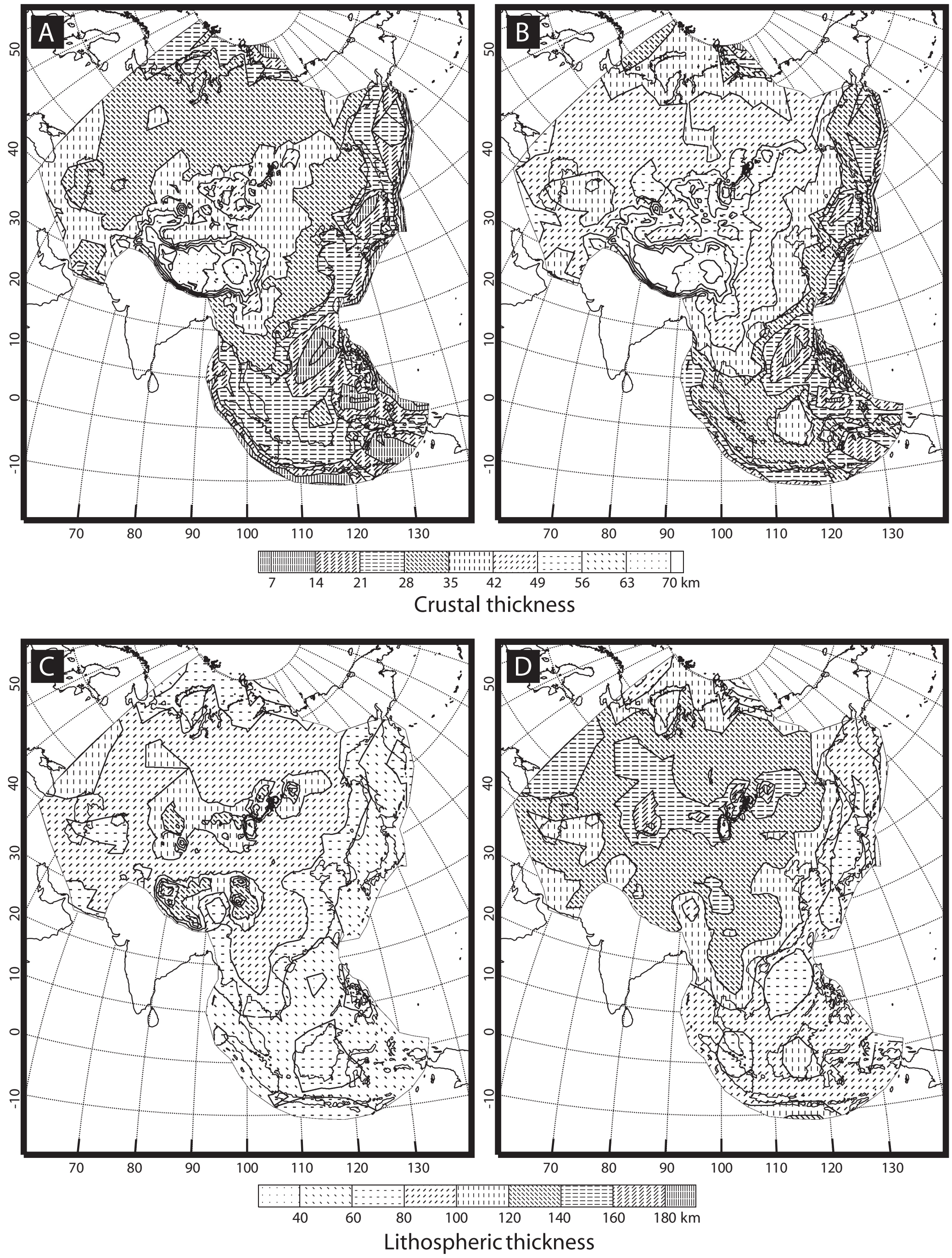

Figure 6. Crustal and lithospheric thicknesses derived from the two sets of thermal parameters tested here (A & C from the weaker rheology, B & D from the stronger rheology).

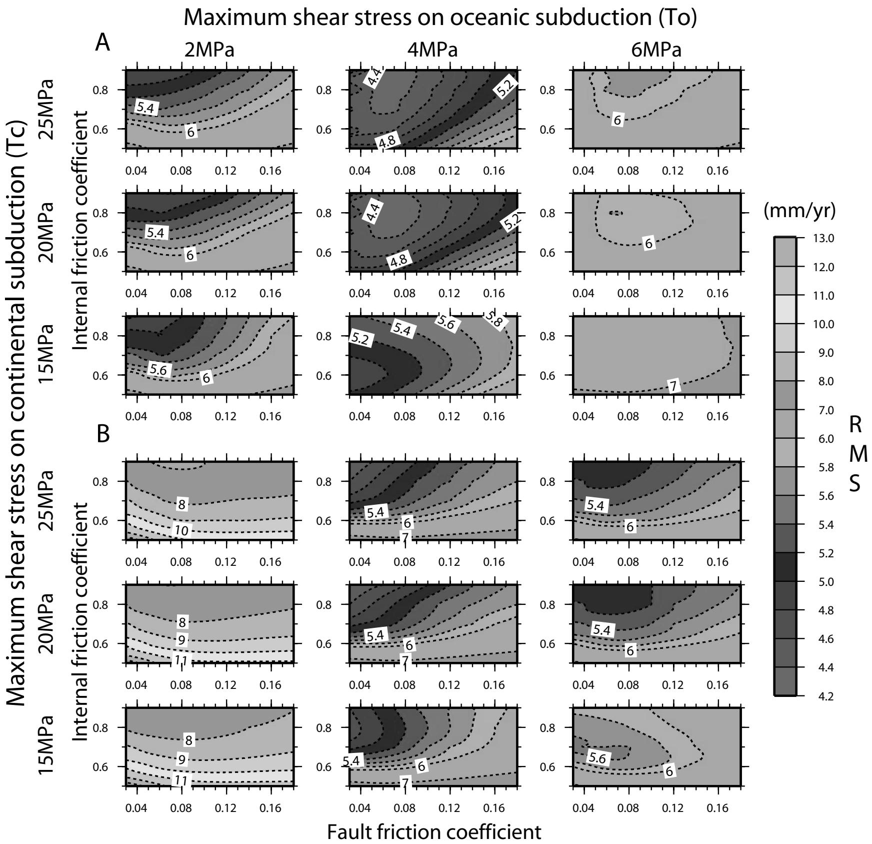

Figure 7. Result of the model parameter grid search for the weaker (A) and stronger (B) lithospheres tested here. Countour lines show the *RMS* of the fit of GPS (Figure 2) to model velocities.

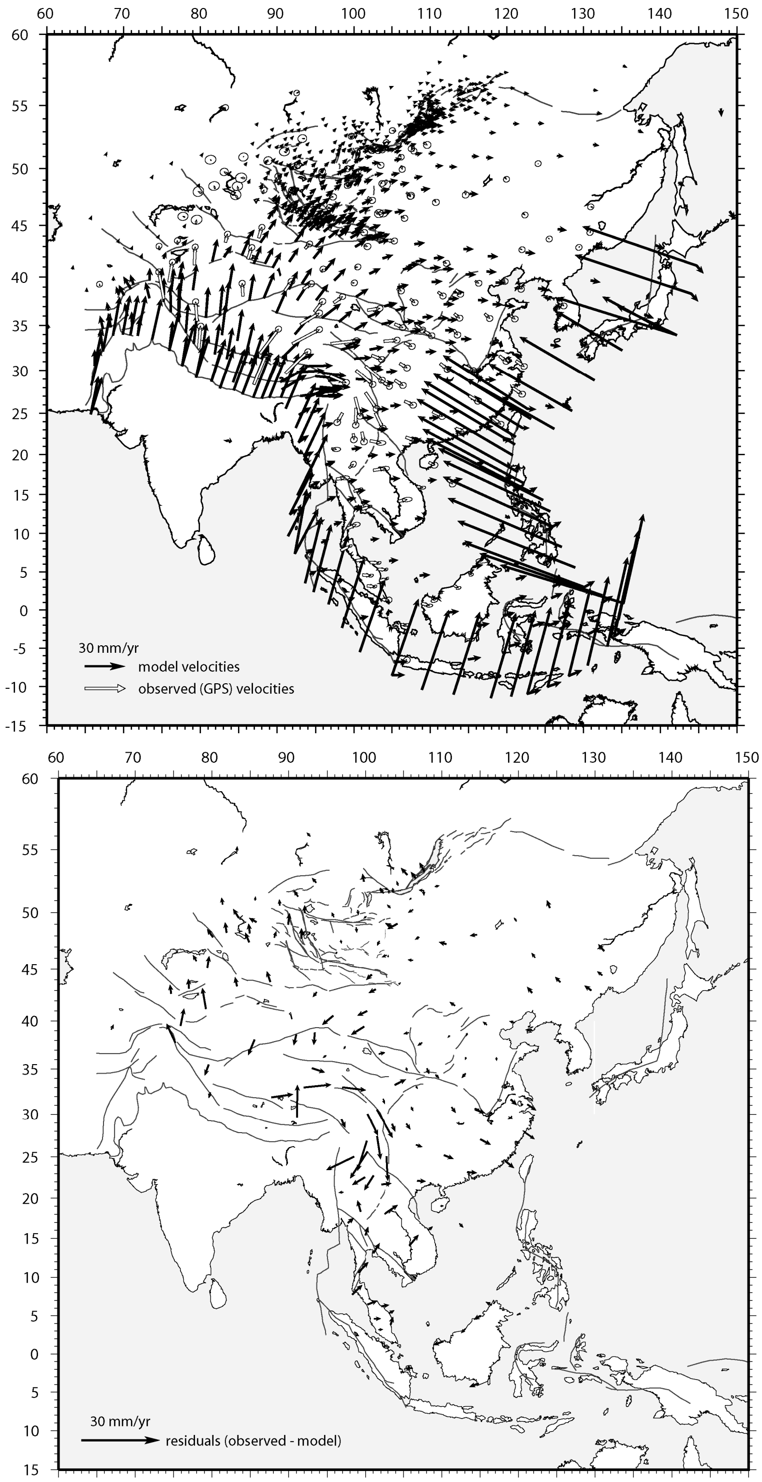

Figure 8. Reference model. A (top) - Model (black arrows) and observed (white arrows) horizontal velocities. B (bottom) - Residuals (observed minus model) velocities. Note the difference in velocity scale between the two figures. Choice of model parameters is explained in text (section 4.2) and summarized in Table 3.

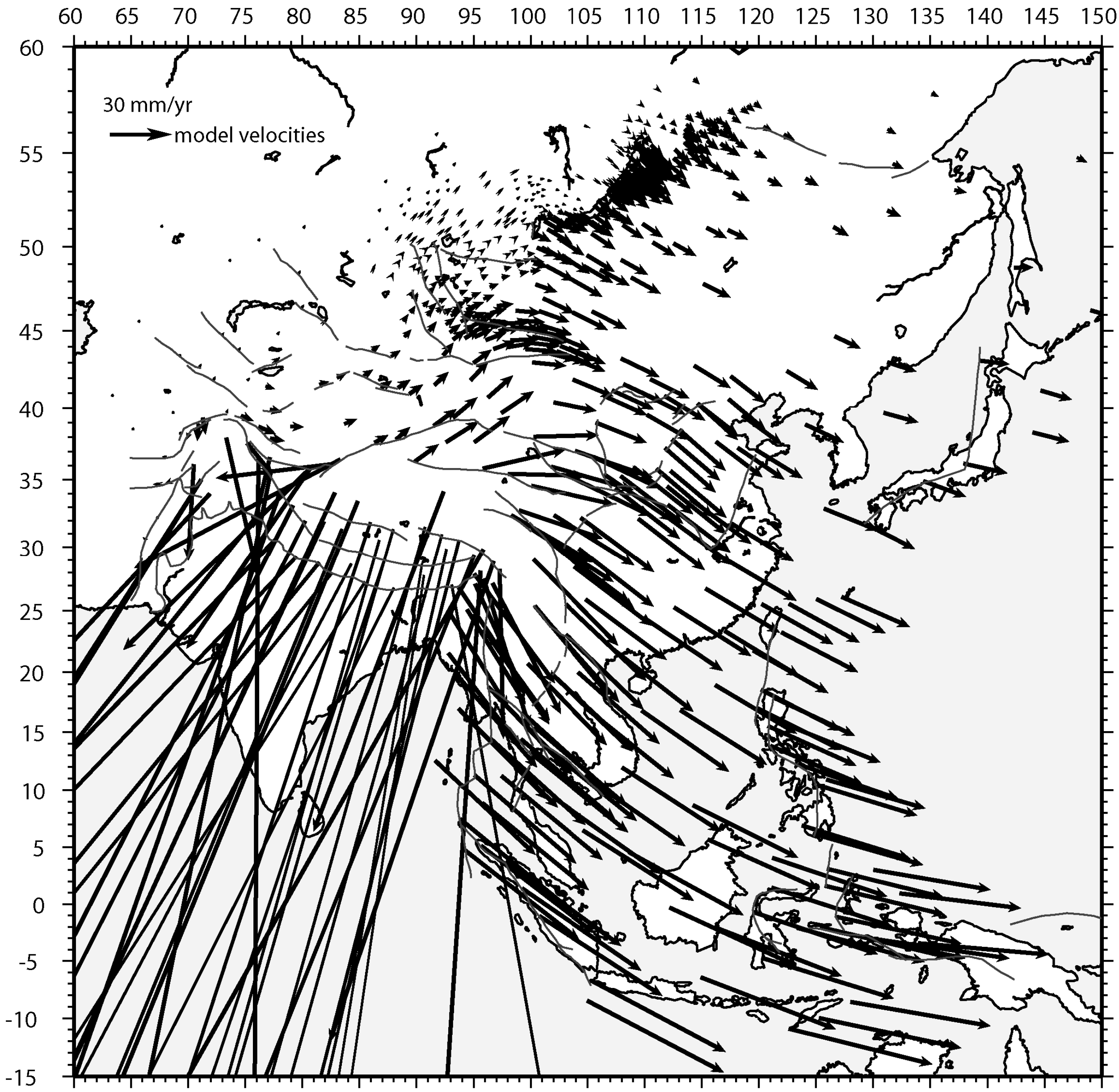

Figure 9. Model 1: Horizontal surface velocities predicted by a model involving only gravitational potential energy gradients. See Table 3 and text (section 5) for a full explanation of the model parameters.

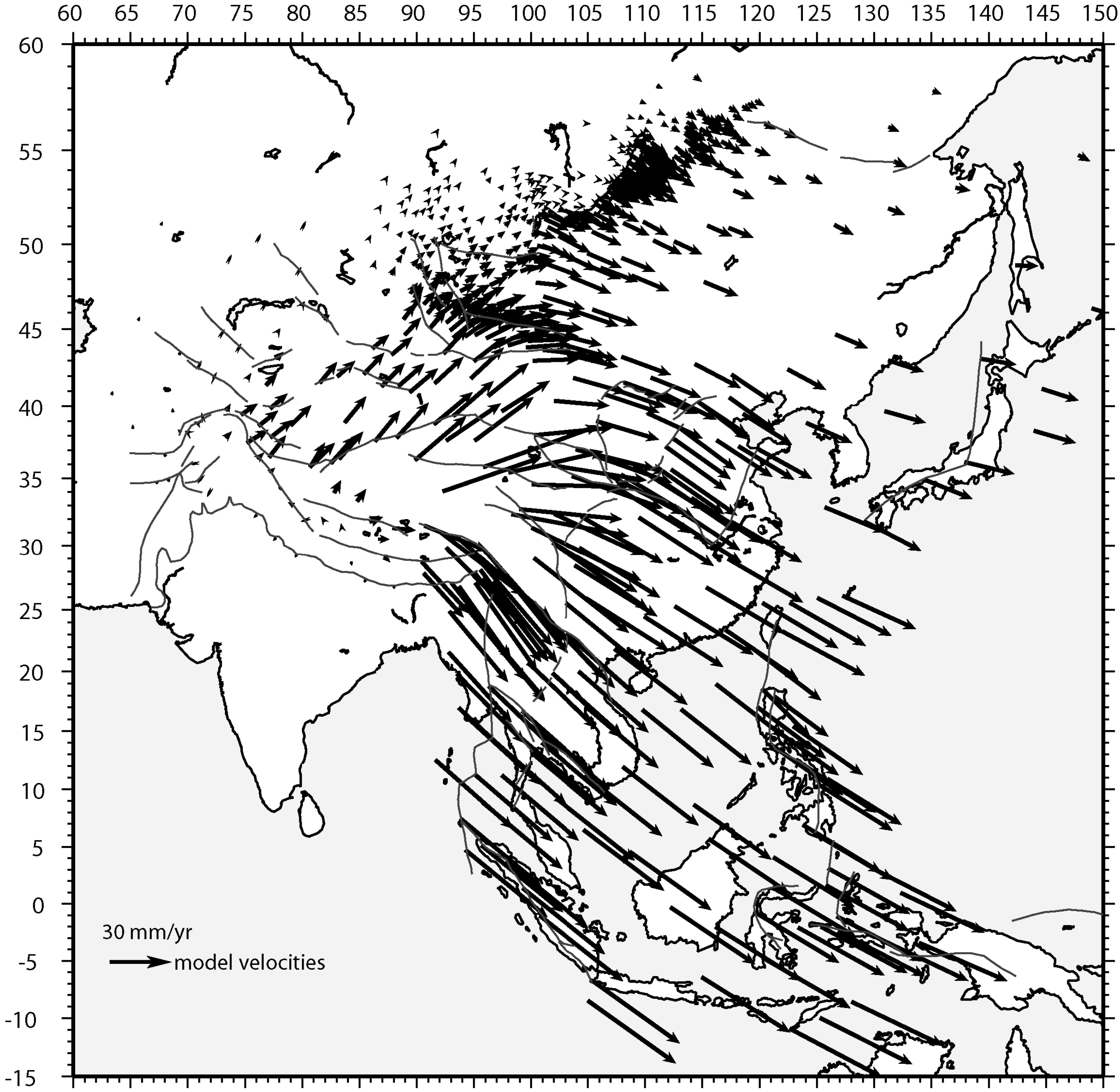

Figure 10. Model 2: Horizontal surface velocities predicted by a model involving gravitational potential energy gradients, a 20 MPa maximum shear traction at continental subductions, and zero velocity along the continental-Eurasia plate boundaries. See Table 3 and text (section 5) for a full explanation of the model parameters.

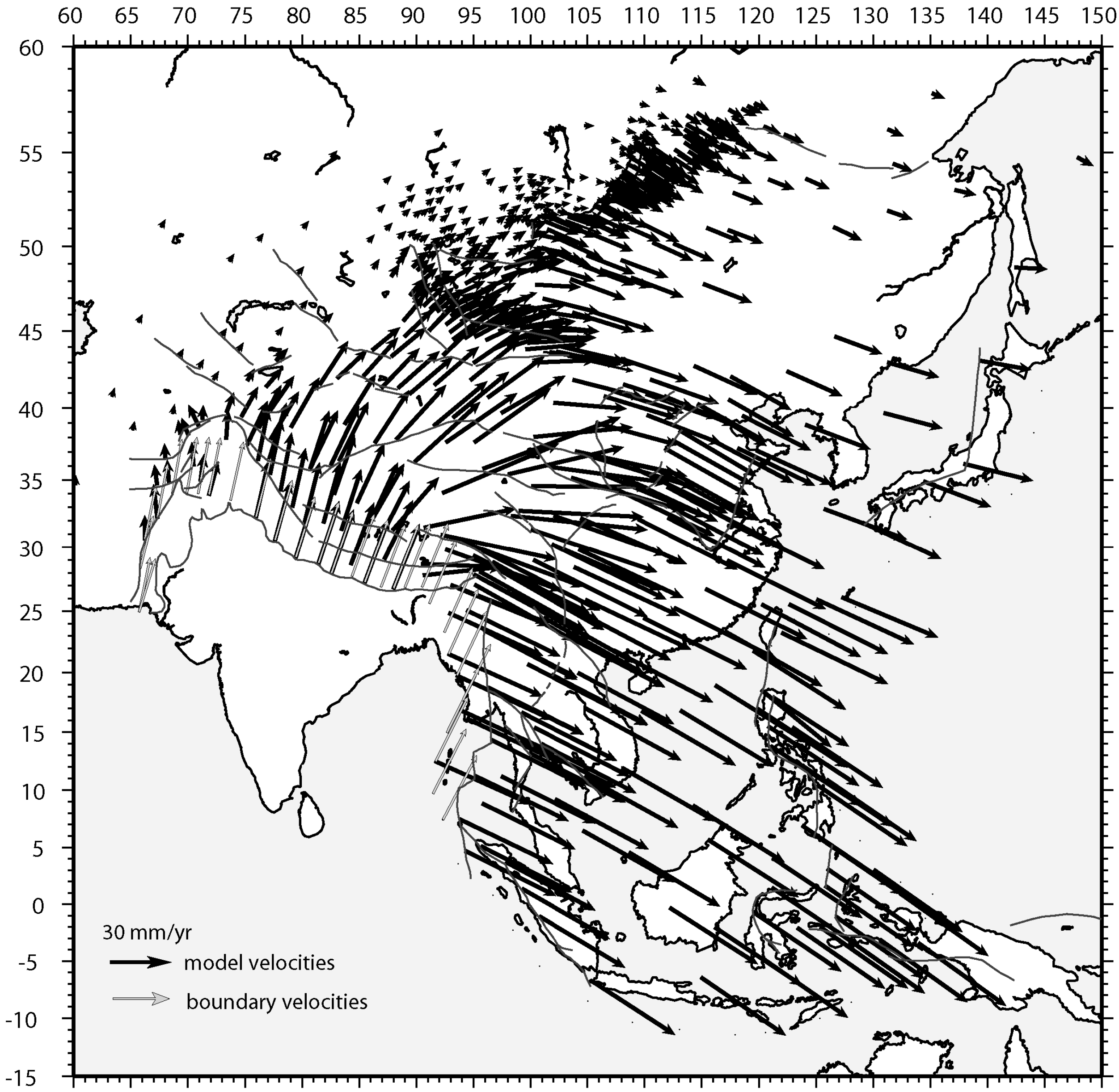

Figure 11. Model 3: Horizontal surface velocities predicted by a model involving gravitational potential energy gradients, a 20 MPa maximum shear traction at continental subductions, and REVEL velocities [*Sella et al.*, 2002] along the continental-Eurasia plate boundaries. See Table 3 and text (section 5) for a full explanation of the model parameters.

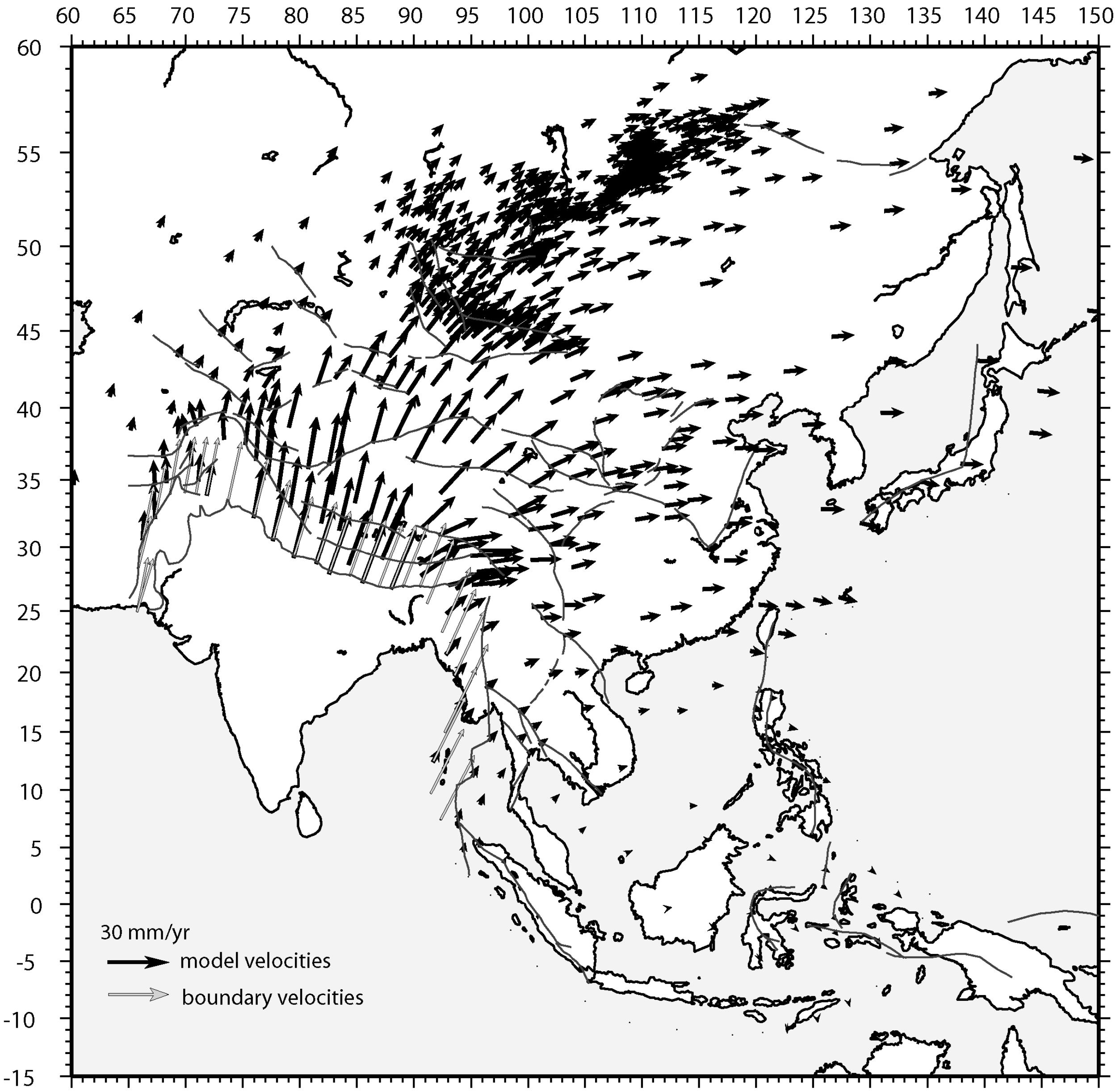

Figure 12. Model 4: Horizontal surface velocities predicted by a model involving gravitational potential energy gradients, a 20 MPa maximum shear traction at continental subductions, a 4 MPa maximum shear traction at the oceanic subduction, and the REVEL velocities [*Sella et al.*, 2002] along the continental-Eurasia plate boundaries. See Table 3 and text (section 5) for a full explanation of the model parameters.

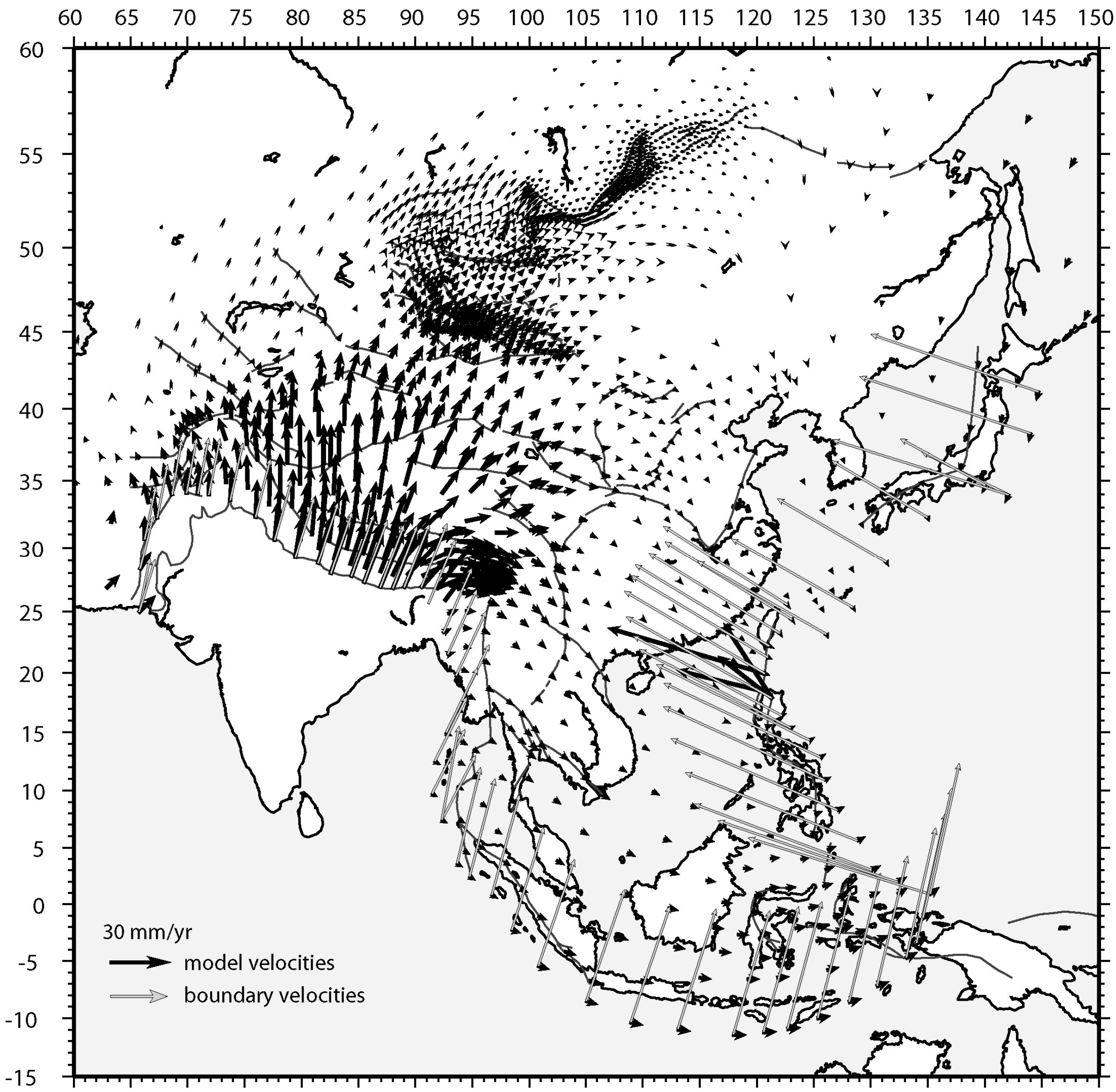

Figure 13. Model 5: Horizontal surface velocities predicted by a model involving boundary and buoyancy forces as in the reference model except that the buoyancy forces result only from gravitational potential energy gradients in the continents. See Table 3 and text (section 6.1) for a full explanation of the model parameters.

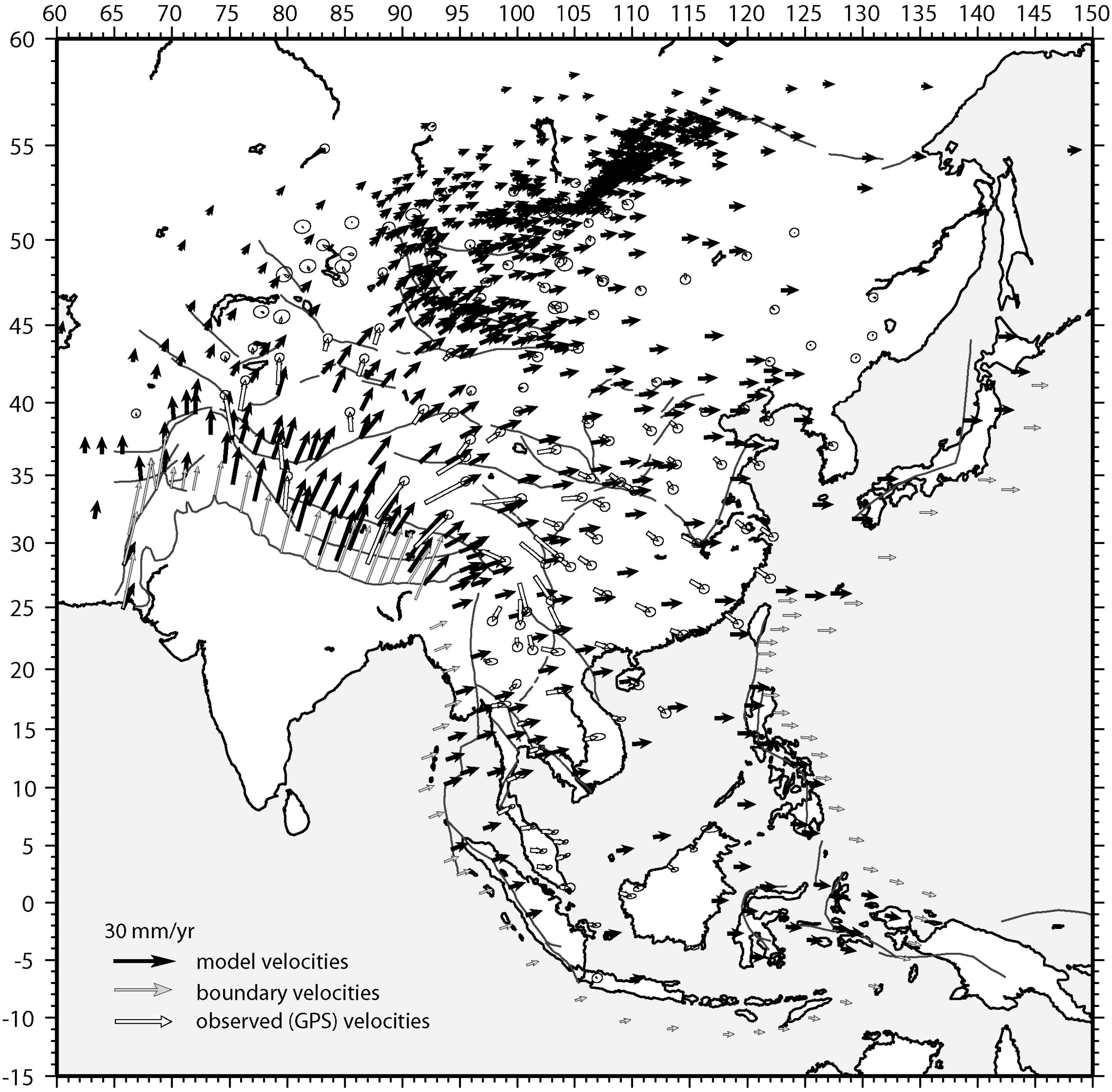

Figure 14. Model 6: Horizontal surface velocities predicted by a model involving no gravitational potential energy gradients, and simulating free motion at oceanic subductions and the India-Eurasia relative plate velocities at the India-Eurasia plate boundary. See text (section 6.2) for a full explanation of the model parameters.

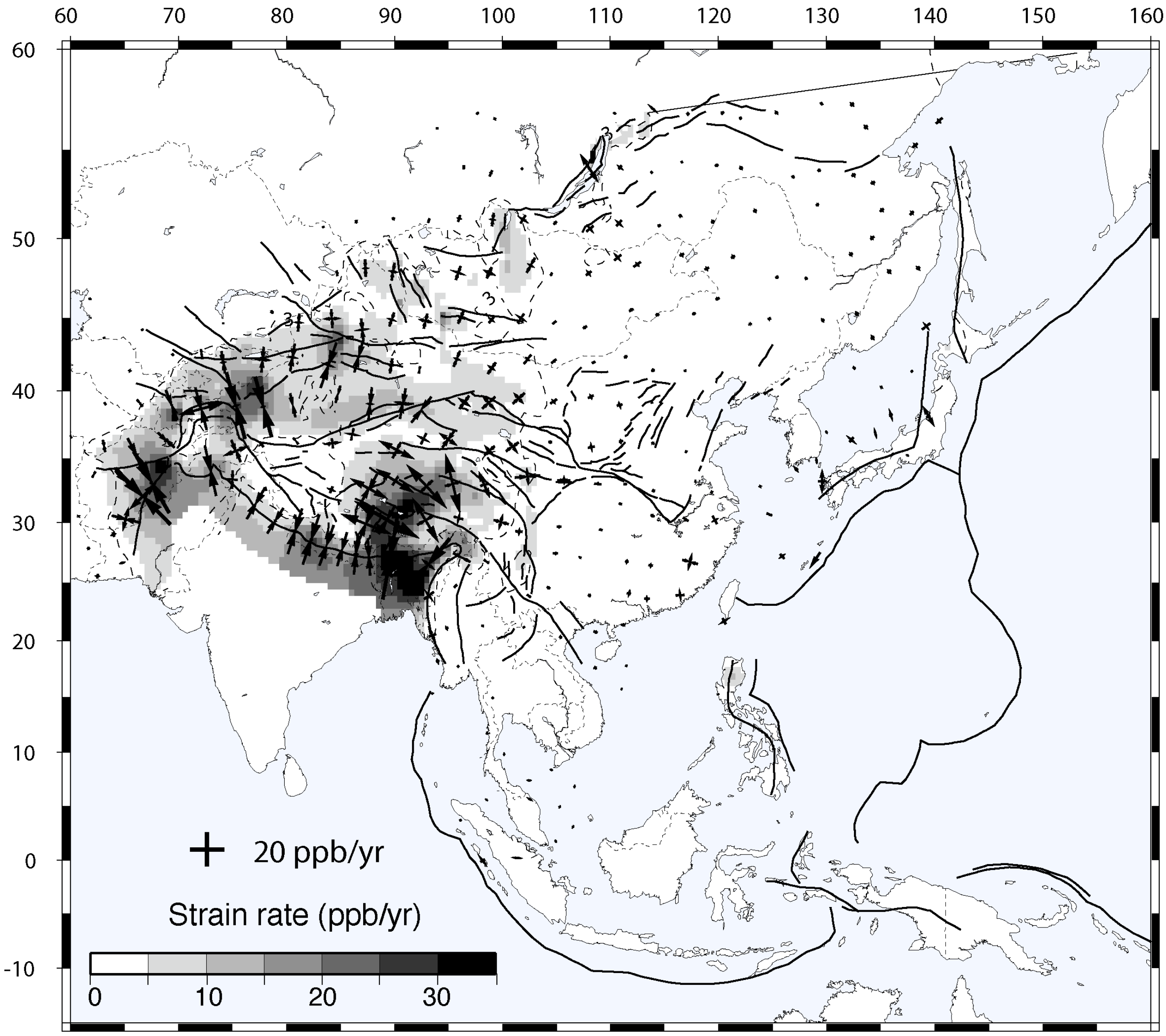

Figure 15. Color background shows the second invariant of the strain rate tensor from the best-fit model (see section 4.2 and Table 3 for full explanation of the model parameters, and Figure 8 for the representation of the best-fit horizontal velocity field). The 3 ppb/yr value is contoured for reference. Black crosses show principal strain rate directions. Convergent arrows indicate compression, divergent arrows indicate extension.

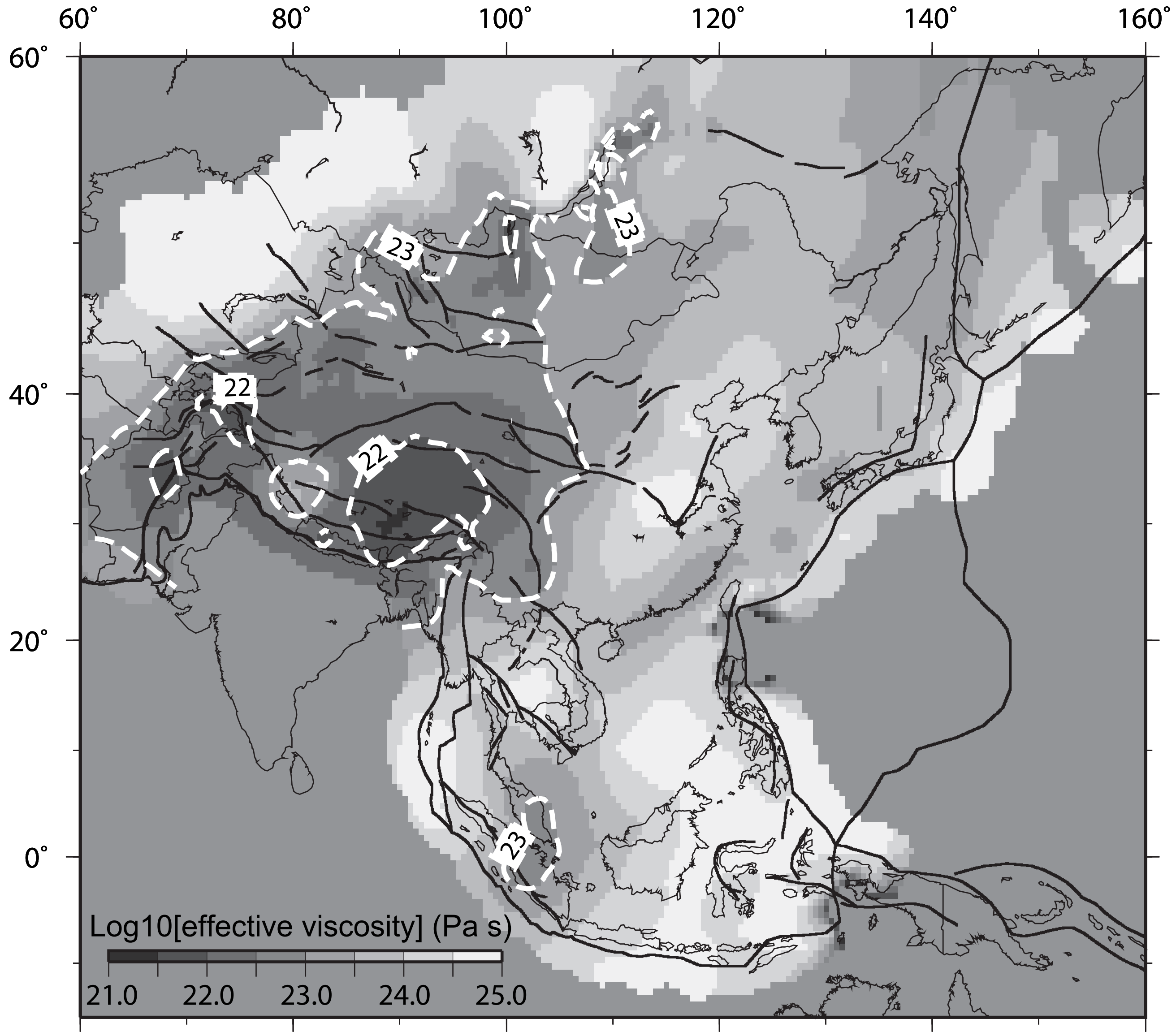

Figure 16. Color background shows the vertically averaged effective viscosity (in Pa s) in the reference model. The amplitude is presented on a logarithmic scale. The 10^{22} and 10^{23} Pa s values are contoured for reference with white dashed lines.

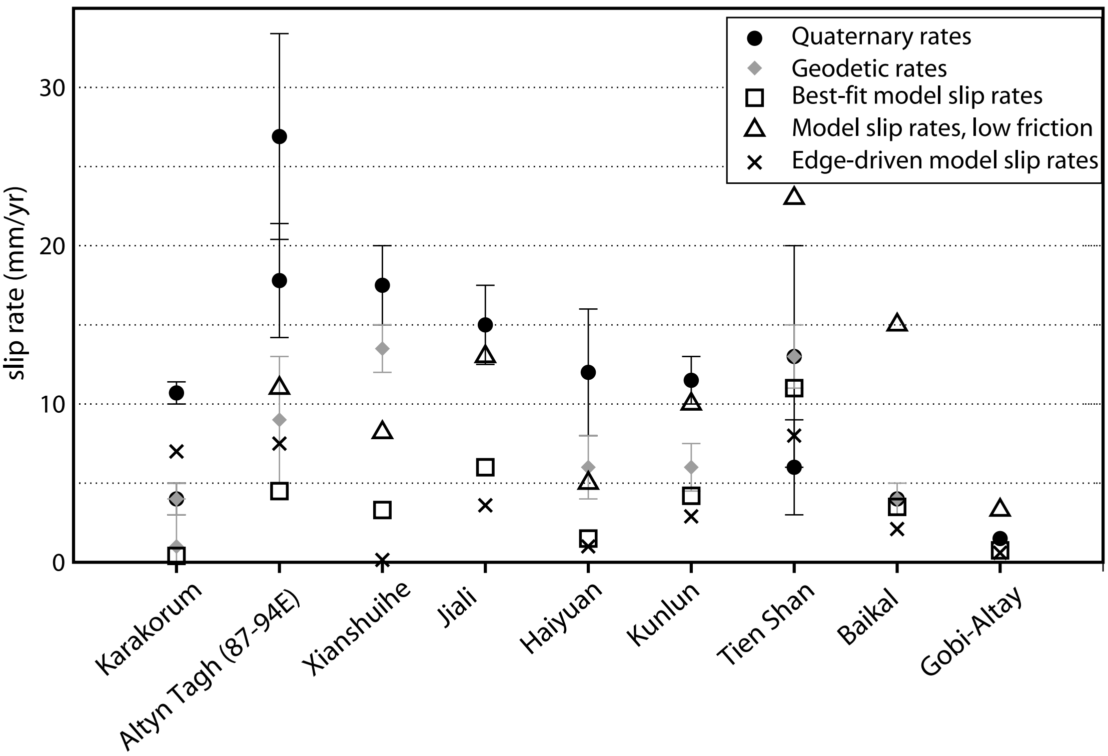

Figure 17. Comparison between Quaternary, geodetic, and model slip rates for major active faults in Asia. Best-fit models (section 4.2) uses a fault friction coefficient of 0.06, low friction model (section 6.4) and edge-driven model (section 6.2) use a fault friction coefficient of 0.01. References for Quaternary and geodetic rates are given in the text.